Spatially localized binary fluid convection in a porous medium

David Lo Jacono, Alain Bergeon, Edgar Knobloch

Spatially localized binary fluid convection in a porous medium

D. Lo Jacono,[1,2,a] A. Bergeon,[1,2] and E. Knobloch[3]
[1]*Université de Toulouse; INPT; UPS; IMFT (Institut de Mécanique des Fluides de Toulouse); Allée Camille Soula, F-31400 Toulouse, France*
[2]*CNRS; IMFT; F-31400 Toulouse, France*
[3]*Department of Physics, University of California at Berkeley, Berkeley, California 94720, USA*

The origin and properties of time-independent spatially localized binary fluid convection in a layer of porous material heated from below are studied. Different types of single and multipulse states are computed using numerical continuation, and the results related to the presence of homoclinic snaking of single and multipulse states.
[doi:10.1063/1.3439672]

I. INTRODUCTION

Stationary spatially localized states are of great interest in the theory of pattern formation. Recently such states have been found in several different types of convection, including binary fluid convection,[1,2] convection in an imposed magnetic field[3–5] and natural doubly diffusive convection.[6–10] Similar states, localized in the cross-stream direction, have been identified in plane Couette flow as well.[11] Despite their physical difference, these systems have two properties in common: they are reversible in space (i.e., invariant under the reflection $x \to -x$, together with the corresponding change in the dependent variables) and exhibit bistability (i.e., there is a parameter regime in which a trivial spatially homogeneous state coexists with a spatially periodic steady state).

The standard picture of systems of this type is most easily described in terms of a simple scalar model equation, the Swift–Hohenberg equation (SHE)

$$u_t = ru - (\partial_x^2 + 1)^2 u + f(u), \tag{1}$$

where $f(u)$ denotes a bistable nonlinearity, either $f(u)=b_2u^2-u^3$ (SH23) or $f(u)=b_3u^3-u^5$ (SH35). Here b_2 and b_3 are positive constants that determine the extent of bistability between the trivial state $u=0$ representing the conduction state and a periodic state $u(x)$ representing convection. Of these two possible choices, SH23 reflects the symmetries of natural doubly diffusive convection in a vertical slot,[8–10] while SH35 reflects the symmetries generally associated with Boussinesq convection in a horizontal layer with identical boundary conditions at the top and bottom.[2,5] Specifically the symmetry $u \to -u$ corresponds to the reflection symmetry in the layer midplane characteristic of these systems. In Fig. 1 we show the results of numerical branch-following for SH35 on a periodic domain with moderately large period Γ.[12,13] The figure shows a branch of spatially periodic steady states (labeled *uniform*) that bifurcates subcritically from the conduction state $u=0$ at $r=0$. The branch is initially unstable but acquires stability at a saddle-node bifurcation where it turns around toward larger r. In the region of bistability, the figure reveals the presence of (four) branches of distinct spatially localized steady states. Two of these are symmetric with respect to $x \to \Gamma - x$ (even parity states), while two are antisymmetric (odd parity states). We refer to even parity states $u(x)$ with a maximum (minimum) at $x=\Gamma/2$ as $\phi=0$ ($\phi=\pi$) states, while odd parity states with maximum (minimum) slope at $x=\Gamma/2$ are referred to as $\phi=\pi/2$ ($\phi=3\pi/2$) states.[12,14] The $\phi=0$ and $\phi=\pi$ states are related by the midplane reflection symmetry $u \to -u$ and so coincide in a diagram such as Fig. 1 that shows the L^2 norm $N \equiv \int_0^\Gamma u^2 dx$ of the solution and likewise for the $\phi=\pi/2$ and $\phi=3\pi/2$ states. These states appear simultaneously in a secondary bifurcation from the branch of uniform amplitude periodic states at small amplitude, and near this bifurcation resemble localized wave packets (profiles *a* and *b*). These branches are unstable until they enter a *snaking* or *pinning* region in which they start to "snake" back and forth, the localized states growing in spatial extent as they do so. Once the domain Γ is almost full, this snaking behavior necessarily terminates, and the branches exit the snaking region and terminate on the periodic states near the aforementioned saddle-node. In this region the solutions resemble even and odd parity *holes*[14,15] in an otherwise spatially periodic pattern (profiles *c* and *d*). As the domain period L increases, the secondary bifurcation creating these states moves to smaller and smaller amplitude, and in the limit $\Gamma \to \infty$, the localized states bifurcate directly from the conduction state, simultaneously with the periodic states. At the same time the termination point approaches closer and closer to the saddle-node.[10] The figure also shows that each snaking branch repeatedly gains and loses stability via saddle-node bifurcations, producing, on an unbounded domain, an infinite multiplicity of coexisting stable states within the pinning region. Secondary bifurcations to pairs of (unstable) branches of asymmetric states are found in the vicinity of each saddle-node; these branches resemble "rungs" that connect the snaking branches and are responsible for the "snakes-and-ladders" structure of the pinning region.[12,14,16]

The above discussion focused on so-called single pulse states, i.e., single localized structures in the available do-

[a]Also at Fluids Laboratory for Aeronautical and Industrial Research (FLAIR), Department of Mechanical and Aerospace Engineering, Monash University, Melbourne, Victoria 3800, Australia.

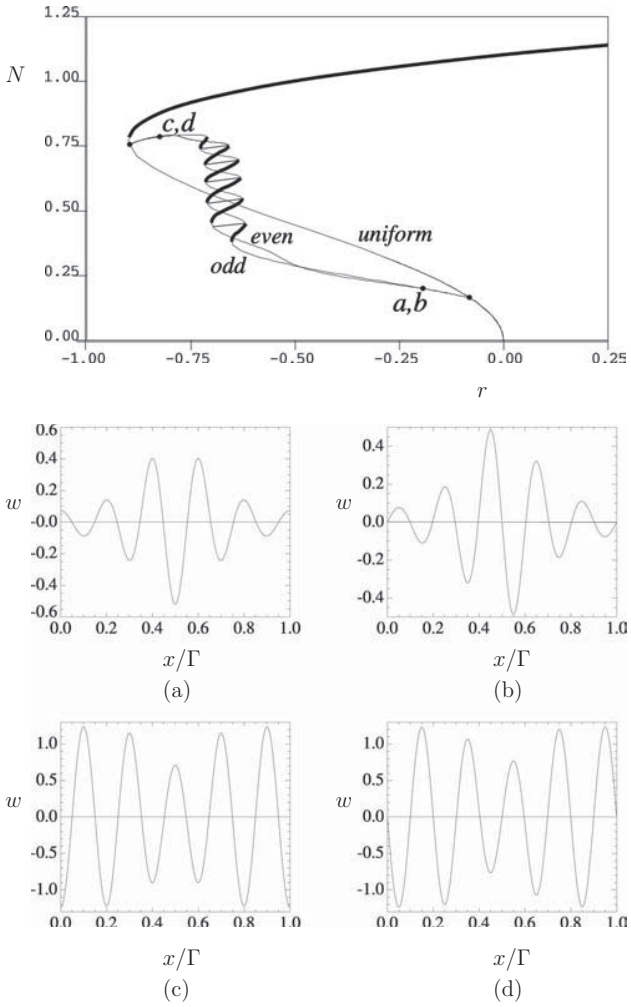

FIG. 1. Bifurcation diagram (top panel) for SH35 showing the L^2 norm of $u(x)$ on a periodic domain with period Γ. Snaking branches of even ($\phi=0,\pi$) and odd ($\phi=\pi/2,3\pi/2$) parity emerge in a secondary bifurcation (solid circle) from a branch of uniform amplitude periodic states with ten wavelengths within Γ and terminate on the same branch in a secondary bifurcation (solid circle) near the saddle-node. Other spatially periodic branches are also present but for clarity are not shown. Other solid circles indicate the location of the profiles $u(x)$ on (a) the $\phi=\pi$ branch at $r=-0.18$, (b) the $\phi=3\pi/2$ branch at $r=-0.18$, (c) the $\phi=0$ branch at $r=-0.83$, and (d) the $\phi=\pi/2$ branch at $r=-0.83$. States (a) and (b) take the form of opposite parity small amplitude wavepackets localized in the center of the domain; states (c) and (d) take the form of opposite parity hole states localized in the center of the domain. Thick (thin) lines indicate stable (unstable) solutions. Parameters: $b_3=2$ and $\Gamma=10\pi$. From J. H. P. Dawes, SIAM J. Appl. Dyn. Syst. **8**, 909 (2009). Copyright © 2009 Society for Industrial and Applied Mathematics. Reprinted with permission. All rights reserved.

main. However, it is clear that we may place multiple localized states in a domain and that such multipulse states will also represent steady solutions of the equation provided these are separated by an integer number of half wavelengths of the oscillations in their tails. Such multipulse states also snake.[17–20]

The origin and properties of the behavior just described are now quite well understood at least for single pulse states in variational systems such as SH23 or SH35.[21–24] In these systems the rung states necessarily correspond to steady solutions.[12,16] This is not so, however, for nonvariational systems. In such systems asymmetric localized states cannot be time-independent, and the rung states correspond to drifting localized waves. On the other hand, since the snaking or pinning region is created through the transversal intersections of certain stable and unstable manifolds,[24–26] its solution structure is believed to be independent of the nature of the system, provided only that it remains bistable and reversible in space. Consequently simple model equations such as SH35 are very useful for interpreting the properties of nonvariational fluid systems, be they binary fluid convection[2,27] or plane Couette flow.[11] Of course, stability properties of the solutions in this region do depend on the details of the system.

In this paper we are interested in exploring properties of multipulse states in a system that shares the symmetry properties of SH35 but not its variational dynamics, focusing on binary fluid convection in a porous medium. We describe the snaking behavior of such states and show that the range of possible behavior is substantially richer than that of the single pulse states. Apart from the importance of porous medium convection in various applications,[28] the associated simplification of the equation of motion allows one to compute many more steady states and do so in larger domains than in other problems of this type. This is, of course, essential for any investigation of multipulse states. We do not consider time-dependent states.

This paper is organized as follows. In the next section we describe briefly the equations we study. In Secs. III and IV we present the results for two different parameter sets obtained using numerical continuation. In Sec. V we provide a theoretical interpretation of the results. We conclude in Sec. VI with a summary of the important results.

II. BINARY FLUID CONVECTION IN A POROUS MEDIUM

Binary fluid convection in a porous medium is characterized by a porosity ϵ and a separation ratio S. The latter measures the separation between the lighter and heavier components of the mixture in an applied temperature gradient. When $S>0$, the heavier component migrates toward the colder boundary; the opposite is the case when $S<0$, the case of interest here, since it results in bistability between the conduction state and a spatially periodic convecting state when the layer is heated from below. In two dimensions the system is described by the dimensionless equations[29]

$$0=-\nabla p+Ra(T+SC)\mathbf{e}_z-\mathbf{u}, \tag{2}$$

$$0=\nabla\cdot\mathbf{u}, \tag{3}$$

$$\frac{\partial T}{\partial t}=-(\mathbf{u}\cdot\nabla)T+\nabla^2 T, \tag{4}$$

$$\epsilon\frac{\partial C}{\partial t}=-(\mathbf{u}\cdot\nabla)C+\tau\nabla^2(C-T), \tag{5}$$

where $\mathbf{u}=(u,w)$ and $\nabla\equiv(\partial_x,\partial_z)$ in (x,z) coordinates, with x in the horizontal direction and z in the vertical direction, T is the temperature, and C is the concentration of the heavier

component of the mixture. The (inverse) Lewis number τ, the Rayleigh number Ra, and the separation ratio S are defined by

$$\tau = \frac{D}{\kappa}, \quad \mathrm{Ra} = \frac{g|\rho_T|\Delta T h}{\lambda \kappa}, \quad S = -S_{\mathrm{Soret}} \frac{\rho_C}{\rho_T} < 0, \tag{6}$$

where λ is the Darcy friction coefficient, κ is the thermal diffusivity, D is the solute diffusivity, $S_{\mathrm{Soret}} < 0$ is the Soret coefficient, g is the gravitational acceleration, and h is the thickness of the layer. In writing these equations we have used the layer thickness h as a unit of length and the vertical thermal diffusion time h^2/κ as the unit of time, together with the linearized equation of state, $\rho(T,C) = \rho_0 + \rho_T(T - T_0) + \rho_C(C - C_0)$, where $\rho_T < 0$, $\rho_C > 0$, and the subscript zero indicates reference values. We suppose that a temperature difference $\Delta T > 0$ is imposed across the system with the lower boundary hotter than the upper boundary; in response the system develops a concentration difference $\Delta C = |S|\Delta T$, with C larger at the bottom than at the top. We use ΔT and ΔC as units of temperature and concentration.

Since the mass flux is proportional to the gradient of $C - T$ the boundary conditions read

$$\begin{aligned} &\text{at } z = 0: \quad w = T - 1 = (C - T)_z = 0, \\ &\text{at } z = 1: \quad w = T = (C - T)_z = 0, \end{aligned} \tag{7}$$

together with periodic boundary conditions (PBCs) with dimensionless period Γ in the x direction. Note that because of the Darcy friction law, we cannot impose boundary conditions on u at $z = 0, 1$. Thus the velocity boundary conditions are "stress-free." This property of the system is beneficial for numerical continuation; the absence of nonlinear terms in the equation of motion (the effective Prandtl number in the medium is infinite) also helps.

In the following we write $T = 1 - z + \Theta$ and $C = 1 - z + \Sigma$ and examine the properties of the equations for u, w, Θ, and Σ. These are invariant under translations in x as well as under two distinct reflections,

$$\begin{aligned} &R_1: \quad (x,z) \to (-x,z), \quad (u,w,\Theta,\Sigma) \to (-u,w,\Theta,\Sigma), \\ &R_2: \quad (x,z) \to (x,1-z), \quad (u,w,\Theta,\Sigma) \to (u,-w,-\Theta,-\Sigma), \end{aligned} \tag{8}$$

where $x = 0$ is an arbitrarily chosen origin, hereafter the center of the domain. The presence of the concentration field Σ precludes the presence of additional symmetries of cosymmetry type,[30] although invariance with respect to Galilean transformations remains. It follows that the equations possess $O(2) \times Z_2$ symmetry (modulo Galilean transformations), where $O(2)$ is the symmetry group of a circle under rotations (translations in x mod Γ) together with the reflection R_1, while Z_2 is the symmetry group $\{1, R_2\}$. The presence of the symmetry R_1 in $O(2)$ implies that the problem is reversible in space, with the reversibility acting by +1. As a result all steady state bifurcations from the conduction state $u = w = \Theta = \Sigma = 0$ as Ra increases are pitchforks of revolution and produce centered spatially periodic states that are either even or odd under spatial reflection. Specifically, even solutions are R_1-symmetric and satisfy

$$\begin{aligned} &[u(-x,z), w(-x,z), \Theta(-x,z), \Sigma(-x,z)] \\ &\quad = [-u(x,z), w(x,z), \Theta(x,z), \Sigma(x,z)], \end{aligned} \tag{9}$$

while odd solutions are $R_2 \circ R_1$-symmetric and satisfy

$$\begin{aligned} &[u(-x,z), w(-x,z), \Theta(-x,z), \Sigma(-x,z)] \\ &\quad = -[u(x,1-z), w(x,1-z), \Theta(x,1-z), \Sigma(x,1-z)]. \end{aligned} \tag{10}$$

Since we are interested in spatially localized convection that asymptotes to the conduction state as $|x| \to \infty$, we need the spatial eigenvalues of this state. Specifically we need to determine values of the Rayleigh number Ra for which the conduction state is hyperbolic, with stable and unstable eigenvalues so that a solution can depart from it as x increases from $-\infty$ and return to it as $x \to +\infty$. Only in this regime can we expect to find exponentially localized structures. To do so we linearize the equations about the conduction state and allow all perturbations to vary as $\exp(i\omega t + \lambda x)$, where ω is real and λ complex. The resulting problem is a sixth order complex-valued eigenvalue problem that can be written in the form

$$\begin{aligned} &(D^2 + \lambda^2) w = \lambda^2 \mathrm{Ra}(\Theta + S\Sigma), \\ &i\omega\Theta = w + (D^2 + \lambda^2)\Theta, \\ &i\epsilon\omega\Sigma = w + \tau(D^2 + \lambda^2)(\Sigma - \Theta), \end{aligned} \tag{11}$$

subject to the boundary conditions $w = \Theta = D(\Sigma - \Theta) = 0$ at $z = 0, 1$. Here $D \equiv d/dz$. A complex-valued eigenvalue problem of this type has two eigenvalues. Given Ra and λ_i, these may be taken to be the frequency ω and the spatial growth rate λ_r.

When $\omega = 0$, this problem has a pair of purely imaginary spatial eigenvalues ($\lambda = \pm i k_c$) of double multiplicity when $\mathrm{Ra} = \mathrm{Ra}_c \approx 47.716\,746\,7$ and $k_c = 3.402\,26$ ($S = -0.01$, $\tau = 0.1$). Moreover, for $\mathrm{Ra} < \mathrm{Ra}_c$, the double multiplicity eigenvalues split and form a quartet of complex eigenvalues, while for $\mathrm{Ra} > \mathrm{Ra}_c$, they also split but remain on the imaginary axis.[8] Thus exponentially localized states can only be present for $\mathrm{Ra} < \mathrm{Ra}_c$. The bifurcation at $\mathrm{Ra} = \mathrm{Ra}_c$ is a Hopf bifurcation with 1:1 resonance in *space* and corresponds to the usual primary bifurcation to steady convection with wavelength $\Lambda_c = 2\pi/k_c$ in the time domain. We mention here that once $\lambda_r \neq 0$, we expect the solution to drift since it is no longer invariant under reflection. This is indeed the case, and in Fig. 2, we show the frequency ω as a function of $\mathrm{Ra}_c - \mathrm{Ra}$ together with λ_r and λ_i. The figure shows that $\lambda_r \propto (\mathrm{Ra}_c - \mathrm{Ra})^{1/2}$, $\lambda_i - k_c \propto \mathrm{Ra}_c - \mathrm{Ra}$, and $\omega \propto (\mathrm{Ra}_c - \mathrm{Ra})^{3/2}$.

III. NUMERICAL METHOD

We compute time-independent spatially localized solutions of Eqs. (2)–(5) with the boundary conditions (7) using a numerical continuation method based on a Newton solver for the time-dependent equations written in terms of Θ and Σ. The implementation of the method follows that of Tuckerman[31] and Mamun and Tuckerman[32] but employs a spectral element method in which the domain

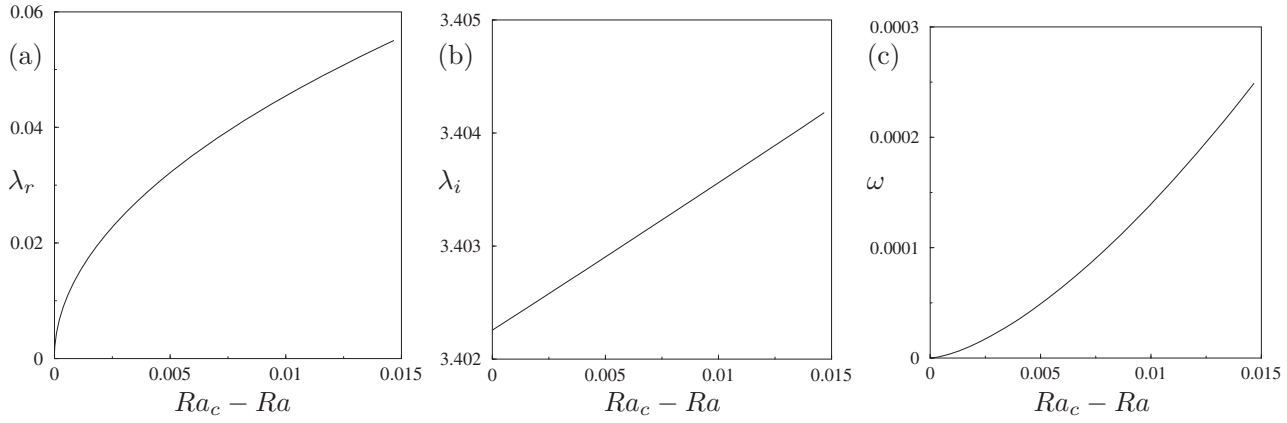

FIG. 2. Solution of the linear stability problem (11). (a) λ_r, (b) λ_i, and (c) ω, all as functions of $\mathrm{Ra}_c - \mathrm{Ra}$. Parameters: $S=-0.01$, $\tau=0.1$, and $\epsilon=1$.

$[0,\Gamma]\times[0,1]$ is decomposed into Ne macroelements of size $[(i-1)\Gamma/\mathrm{Ne}, i\Gamma/\mathrm{Ne}]\times[0,1]$, where Ne is the number of spectral elements and $i\in\{1,\ldots,\mathrm{Ne}\}$. In each element, the fields are approximated by a high order interpolant through the Gauss–Lobatto–Legendre points.[33] The Newton solver uses a first order time-stepping scheme for Eqs. (4) and (5). The diffusive linear part of the equations is treated implicitly, while the nonlinear part is treated explicitly. Since the latter requires the velocity, a Poisson problem is formulated for the pressure p by combining Eqs. (2) and (3). This problem is solved subject to Neumann boundary conditions (NBCs) as obtained from the projection of Eq. (2) on $\mathbf{e}_z$ using the fact that $\mathbf{u}\cdot\mathbf{e}_z=\Theta=0$ on $z=0,1$. With p known, Eq. (2) determines the velocity field $\mathbf{u}$. Each time step therefore requires the inversion of two Helmholtz problems and one Poisson problem. This is carried out using a Schur factorization procedure on the weak form of the equations,[33] a procedure that ensures the periodicity of the unknowns and their first derivative in the x-direction.

The continuation is initialized using small amplitude localized solutions computed from weakly nonlinear analysis near $\mathrm{Ra}=\mathrm{Ra}_c$.[8] Since the primary bifurcation is subcritical, these solutions are present in $\mathrm{Ra}<\mathrm{Ra}_c$.

Below we present results for the following parameter combinations: (a) $\tau=0.5$ and $S=-0.1$ as used by Charrier-Mojtabi *et al.*[34] and (b) $\tau=0.05$ and $S=-0.01$. The relatively large value of τ in (a) avoids thin concentration boundary layers allowing more detailed computational results. On the other hand, the parameter choice (b) represents physically more relevant parameter values. The porosity ϵ, which we take to be $\epsilon=1$, affects only the stability properties of the steady solutions. To simplify the computations we impose the symmetries R_1 or $R_2\circ R_1$ on all solutions. Throughout the paper we use an aspect ratio (spatial period) given by $\Gamma=20(2\pi/k_P)$, where $k_P=3.75$ is close to the infinite domain critical wavenumber for onset of steady convection, $k_c\approx 3.747$ in case (a) and $k_c\approx 3.687$ in (b). Consequently we expect the first primary bifurcation to lead to a periodic stationary state with $n_c=20$ wavelengths in the periodic box, and this is indeed the case.

IV. RESULTS: $\tau=0.5$ AND $S=-0.1$

In a finite but large periodic domain with aspect ratio $\Gamma=20(2\pi/k_P)$, the first primary bifurcation occurs at $\mathrm{Ra}_{20}=66.75\approx\mathrm{Ra}_c$ and produces a subcritical branch of periodic states with $n_c=20$. This bifurcation is followed in $\mathrm{Ra}>\mathrm{Ra}_{20}$ by primary bifurcations with $n\neq n_c$. In the following we refer to the resulting branches of periodic states as P_n. Thus P_{21} bifurcates at $\mathrm{Ra}_{21}=67.01$, P_{19} at $\mathrm{Ra}_{19}=67.03$, etc. Figure 3 shows the P_n branches for $17\le n\le 22$ in terms of their dimensionless kinetic energy $\mathcal{E}\equiv\frac{1}{2}\int_0^\Gamma\int_0^1(u^2+w^2)dxdz$. The bifurcations to all P_n are subcritical. As a result each branch undergoes a saddle-node bifurcation before turning around toward larger values of Ra. The saddle-node on P_{20} is found at $\mathrm{Ra}=52.84$; however, as shown in Fig. 3, subsequent branches extend to lower values of Ra despite bifurcating from the conduction state at larger values of Ra. Thus P_{17} has a saddle-node at $\mathrm{Ra}=51.35$, while P_{18} has a saddle-node at $\mathrm{Ra}=51.56$.

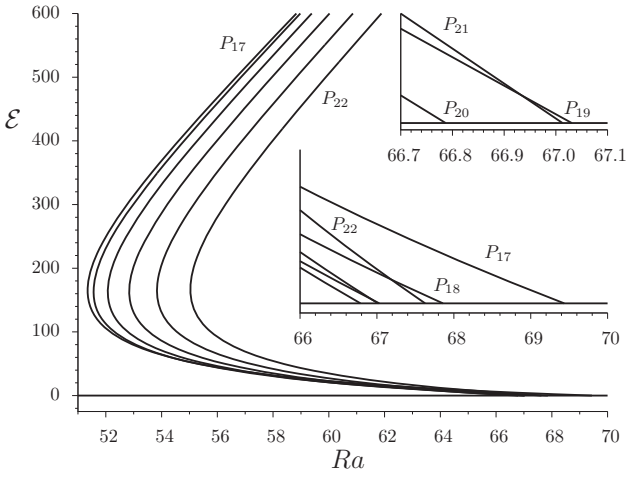

FIG. 3. Bifurcation diagram showing the branches $P_n(n\in[17,22])$ of periodic states as a function of the Rayleigh number Ra. Parameters: $\tau=0.5$ and $S=-0.1$.

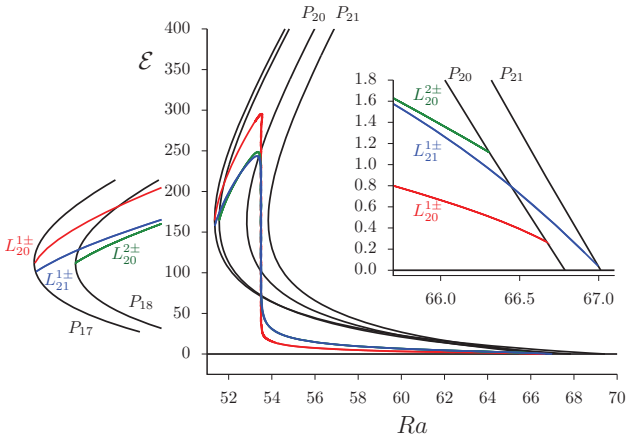

FIG. 4. (Color online) Bifurcation diagram showing some of the secondary branches of localized states connecting the various periodic states. The insets show enlargements of the small amplitude behavior near onset and the termination of the secondary branches near the saddle-nodes on P_{17} and P_{18}. The snaking region near Ra=53.5 is not resolved on the scale of this plot. Parameters: τ=0.5 and S=−0.1.

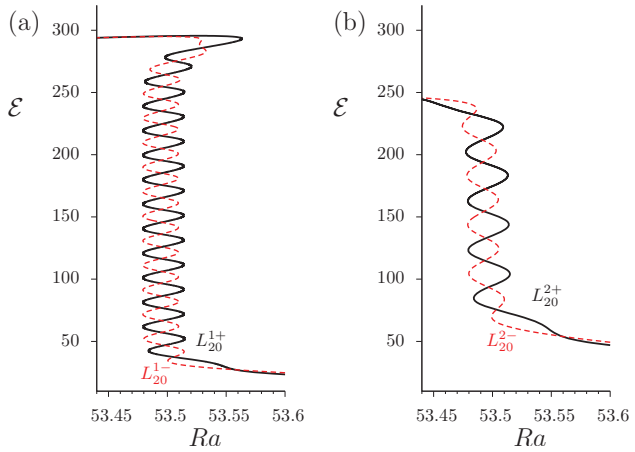

FIG. 5. (Color online) Detail of the snaking region in Fig. 4. (a) Snaking of the single pulse states $L_{20}^{1\pm}$; solid (dashed) line represents even (odd) parity states L_{20}^{1+} (L_{20}^{1-}). The L_{20}^{1-} snaking region is narrower than the L_{20}^{1+} snaking region. (b) Snaking of equally spaced two-pulse states with phases $\phi=(0,0)$ (L_{20}^{2+}, solid line) and $\phi=(\pi/2,\pi/2)$ (L_{20}^{2-}, dashed line). The L_{20}^{2-} snaking region is narrower than the L_{20}^{2+} snaking region. Parameters: τ=0.5 and S=−0.1.

A. Single pulse states

Figure 4 shows the n=17, 18, 20, and 21 periodic branches together with three families of spatially localized structures, labeled $L_{20}^{1,2\pm}$ and $L_{21}^{1\pm}$. Branches labeled $L_{20}^{1\pm}$ bifurcate from P_{20} first, i.e., closest to the primary bifurcation, while those labeled $L_{20}^{2\pm}$ bifurcate next. Likewise, branches labeled $L_{21}^{1\pm}$ are the first to bifurcate from P_{21}. The $L_{20}^{1\pm}$ states are single pulse states, while both $L_{20}^{2\pm}$ and $L_{21}^{1\pm}$ correspond to (different types of) two-pulse states. At small amplitude the $L_{20}^{1\pm}$ states take the form of wave packets with a slowly varying envelope, the + state being even (i.e., invariant under R_1) and the − state being odd (i.e., invariant under $R_2\circ R_1$). In this regime the corresponding solution branches are essentially indistinguishable. However, as each branch in a pair is followed toward smaller values of Ra and hence larger amplitude, the packets become more and more localized, and the branches split apart. Once their amplitude and width become comparable to the amplitude and wavelength of the coexisting periodic states, the branches enter the so-called snaking or pinning region and begin to snake back and forth [see Fig. 5(a)] as each structure acquires additional rolls, one on either side, as one passes from saddle-node to the corresponding saddle-node higher up. Once the domain is almost full, the snaking ceases, and the $L_{20}^{1\pm}$ branches exit the snaking region and terminate together near the saddle-node on P_{17} (see Fig. 4). Near this point the solutions take the form of a slowly modulated wavetrain as the "holes" between the periodically spaced localized structures gradually fill in.

In the present problem there are in fact four branches of single pulse localized structures. This is a consequence of the midplane reflection symmetry R_2 of the present problem.[12] Two of these solutions are even with respect to R_1 [cf. Eq. (9)], and we refer to them using their spatial phase ϕ=0, π or simply as L^+. The states with ϕ=0 have maxima on the symmetry line x=0, while states with $\phi=\pi$ have the opposite sign and so have minima at x=0. The remaining two branches are odd under reflection [cf. Eq. (10)] with spatial phase $\phi=\pi/2$ and $3\pi/2$; states with $\phi=\pi/2$ have maximum positive slope at x=0, while those with $\phi=3\pi/2$ have maximum negative slope at x=0. We refer to states of this type as L^-. This solution structure is identical to that found in binary fluid convection between two identical (no-slip) horizontal boundaries[2,27] and is reproduced by SH35 (Fig. 1). Note that, like the L^2 norm N in Fig. 1, the energy $\mathcal{E}$ used in Fig. 4 does not distinguish between ϕ=0 and π or between $\phi=\pi/2$ and $3\pi/2$. Figure 6 shows sample profiles as one proceeds from small to large amplitude along the even parity $\phi=\pi$ branch, while Fig. 7 shows the corresponding results for the odd parity $\phi=\pi/2$ branch. In the case shown, all four branches are born together on P_{20}, and all four terminate together on P_{17}; this is not necessarily always the case.[10,13]

We mention that in nonvariational problems of the type studied here, the $L^\pm$ branches are connected by "rung states." These consist of states that are neither even nor odd and hence take the form of *drifting* localized states; we have not computed these nonstationary states.

B. Two-pulse states

The snaking region contains many additional states as well. Figure 5(b) shows a second pair of snaking branches labeled $L_{20}^{2\pm}$. These also bifurcate from the first primary branch P_{20} but in a subsequent secondary bifurcation (see Fig. 4) and terminate together on the branch P_{18} (Fig. 4). One of these consists of two equidistant copies of the single pulse ϕ=0 state [branch L_{20}^{2+} in Fig. 5(b)], while the other consists of two equidistant copies of the single pulse $\phi=\pi/2$ state [branch L_{20}^{2-} in Fig. 5(b)]. Figures 8 and 9 show the corresponding solution profiles at successive saddle-nodes along the left boundary of the pinning region. We see that these states are equivalent to a single pulse state on a domain of period $\Gamma/2$; it is for this reason that they bifurcate from P_{20} at larger amplitude than the corresponding states on a domain of period Γ and also the reason they terminate on a

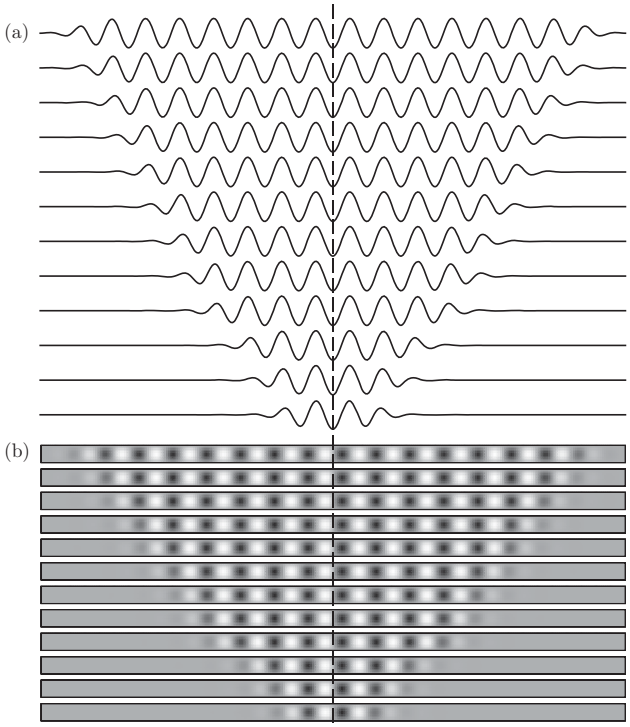

FIG. 6. (a) Line plots showing the midplane vertical velocity $w(x,z=1/2)$ along the branch of even parity $\phi=\pi$ localized states computed at the leftmost saddle-nodes in the snaking region; see L_{20}^{1+} in Fig. 5(a). The dashed line indicates the symmetry axis of the localized states. (b) The streamfunction at the same locations. Light (dark) shading indicates clockwise (counterclockwise) flow. Parameters: $\tau=0.5$ and $S=-0.1$.

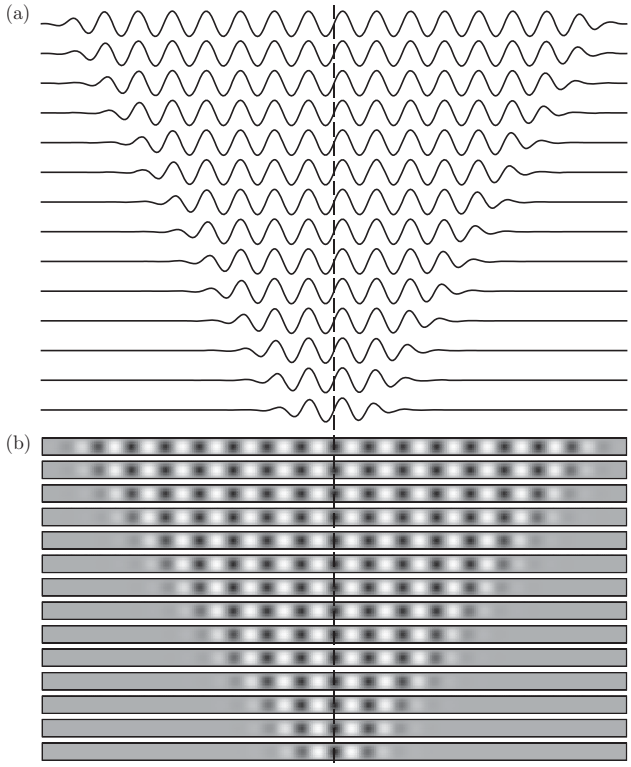

FIG. 7. (a) Line plots showing the midplane vertical velocity $w(x,z=1/2)$ along the branch of odd parity $\phi=\pi/2$ localized states computed at the leftmost saddle-nodes in the snaking region; see L_{20}^{1-} in Fig. 5(a). The dashed line indicates the symmetry axis of the localized states. (b) The streamfunction at the same locations. Light (dark) shading indicates clockwise (counterclockwise) flow. Parameters: $\tau=0.5$ and $S=-0.1$.

different branch of periodic states. Since the available domain is only $\Gamma/2$ there are roughly half as many turns in the snake before the domain fills up and snaking terminates.

Snaking branches, labeled $L_{21}^{1\pm}$, bifurcate from P_{21} as well (Fig. 4). Once again there is a pair of branches, and this time these terminate together on P_{17} (Fig. 4). As expected,[10] this termination point is further from the saddle-node on P_{17} than the termination point of $L_{20}^{1\pm}$. Figure 10 shows the resulting snaking branches. The branch L_{21}^{1+} consists of bound states of two equidistant identical even parity states, with $\phi=0$, π (see Fig. 11), while branch L_{21}^{1-} consists of bound states of two equidistant identical odd parity states, with $\phi=\pi/2$ and $3\pi/2$, such that the overall structure retains reflection symmetry with respect to the centerline $x=0$ (see Fig. 12).

C. Secondary bifurcations from the snaking branches

We have already mentioned that the two single pulse branches $L_{20}^{1\pm}$ are connected by a series of rungs consisting of asymmetric drifting pulses forming the so-called snakes-and-ladders structure of the snaking region. High up the snaking structure, these interconnecting branches bifurcate from the $L_{20}^{1\pm}$ exponentially close to the saddle-nodes, much as in the SHE.[12,16] However, there are bifurcations to stationary states as well. Such states must again be even or odd under reflection, and such states bifurcate from $L_{21}^{1\pm}$. In this section we only consider states of this type that have even parity.

Figure 13 shows the $L_{21}^{1\pm}$ snaking branches that bifurcate from P_{21}. In addition, Fig. 13 shows (in blue) a branch of solutions that is quite different from any found in the SHE. Here a new branch of two-pulse states bifurcates off the snaking two-pulse branch L_{21}^{1-} at the point labeled by * [Fig. 13(a)]. The branch follows a rung state and then a portion of the L_{21}^{1+} branch as if to form an isola. However, the isola remains incomplete since the branch only follows a part of the next rung state before turning around and producing a cusplike feature. Figure 14 shows a sequence of solution profiles in this region. These cusplike features occur repeat-

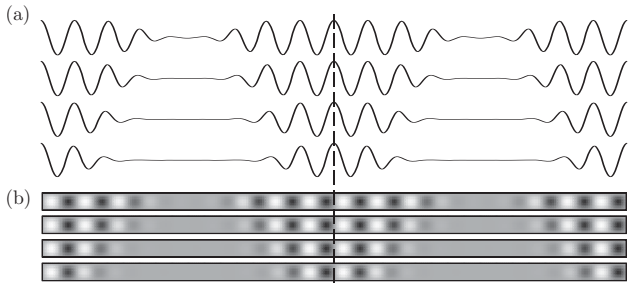

FIG. 8. (a) Line plots showing the midplane vertical velocity $w(x,z=1/2)$ along the branch of bound states of two even parity $\phi=0$ localized states computed at the leftmost saddle-nodes in the snaking region, see L_{20}^{2+} in Fig. 5(b). The dashed line indicates the symmetry axis of the localized states. (b) The streamfunction at the same locations. Light (dark) shading indicates clockwise (counterclockwise) flow. Parameters: $\tau=0.5$ and $S=-0.1$.

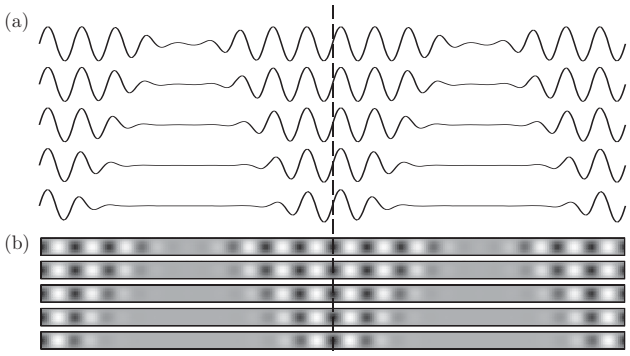

FIG. 9. (a) Line plots showing the midplane vertical velocity $w(x,z=1/2)$ along the branch of bound states of two odd parity $\phi=\pi/2$ localized states computed at the leftmost saddle-nodes in the snaking region; see L_{20}^{2-} in Fig. 5(b). The dashed line indicates the symmetry axis of the localized states. (b) The streamfunction at the same locations. Light (dark) shading indicates clockwise (counterclockwise) flow. Parameters: $\tau=0.5$ and $S=-0.1$.

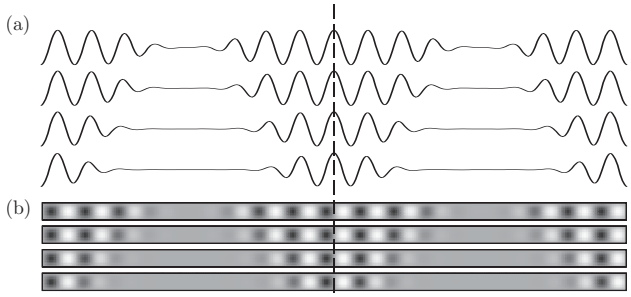

FIG. 11. (a) Line plots showing the midplane vertical velocity $w(x,z=1/2)$ along the branch of bound states of two even parity localized states with $\phi=0$, π computed at the leftmost saddle-nodes in the snaking region; see L_{21}^{1+} in Fig. 10. The dashed line indicates the symmetry axis of the localized states. (b) The streamfunction at the same locations. Light (dark) shading indicates clockwise (counterclockwise) flow. Parameters: $\tau=0.5$ and $S=-0.1$.

edly as one proceeds down the branch, following close to the L_{21}^{1+} branch. The branch ultimately reaches very small amplitude at a saddle-node labeled 9 [Fig. 13(c)] before it starts to snake back upward, this time following the L_{21}^{1-} branch. During this phase the branch again makes abortive attempts at completing isolas by making excursions along the rung states, but this time the excursions are shorter. The branch eventually terminates near saddle-node 16 on the same branch that it bifurcated from, also labeled by * [Fig. 13(a)]. The overall structure of the branch thus takes the form of an "unzipped" snake. Figure 15 shows sample solution profiles along this branch. The solution consists at small amplitude of a pair of narrow single pulse states of type $(\pi/2,3\pi/2)$ near location 9; as one goes from 9 to 1, both pulses turn into type (0,0) and grow in width but do so while maintaining the void between them. As a result the growth is markedly asymmetric. Indeed, both pulses grow from the inner region, and as new oscillations are added at the location of the inner fronts, existing oscillations are gradually pushed outward (Fig. 15). The approach to the (0,0) state is unexpected and not understood; after all, Fig. 13(b) suggests that the branch follows L_{21}^{1+}, i.e., that the states along it between locations 2 and 9 should resemble $(0,\pi)$. In contrast, from 9 to 16, the pulses take the form $(\pi/2,3\pi/2)$, as they should, but again grow by nucleating new structure at the inner fronts. This process only terminates once each pulse has grown sufficiently that their centers are separated by $\Gamma/2$ (see location 16, for example), and the solution turns into a regular two-pulse state L_{21}^{1-}.

Figure 13 also shows a second branch connecting L_{21}^{1-} to itself. This branch, drawn in green, has the shape of the letter Z and evidently forms in the upper reaches of the snaking diagram by the same process as that leading to the branch drawn in blue. This disconnection appears to be a consequence of an almost full domain. The solution profiles along this branch are shown in Fig. 16 and resemble bound states of type $(\pi/2,3\pi/2)$ as expected.

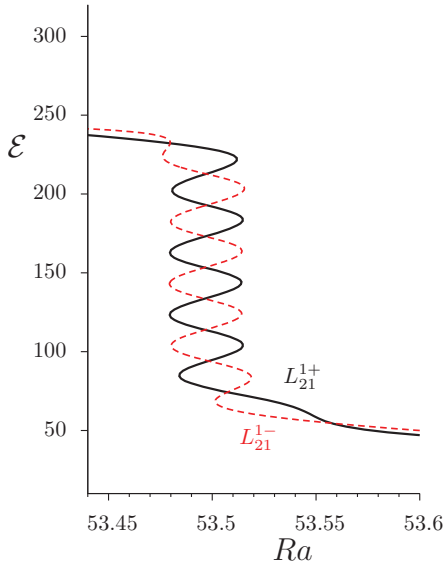

FIG. 10. (Color online) Further detail of the snaking region in Fig. 4. Snaking of two-pulse states with phases $\phi=(0,\pi)$ (L_{21}^{1+}, solid line) and $\phi=(\pi/2,3\pi/2)$ (L_{21}^{1-}, dashed line). The widths of the two snaking regions are the same. Parameters: $\tau=0.5$ and $S=-0.1$.

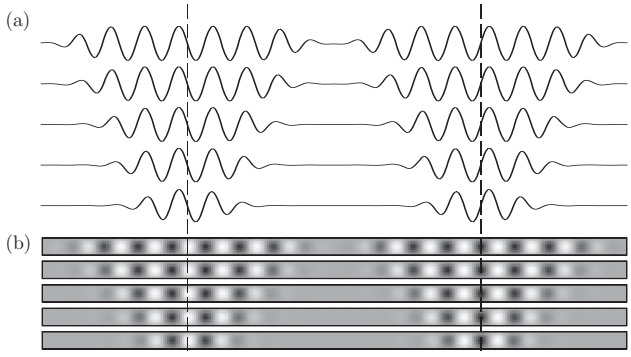

FIG. 12. (a) Line plots showing the midplane vertical velocity $w(x,z=1/2)$ along the branch of bound states of two odd parity localized states with $\phi=\pi/2$ and $3\pi/2$ computed at the leftmost saddle-nodes in the snaking region; see L_{21}^{1-} in Fig. 10. The dashed line indicates the symmetry axis of the localized states. (b) The streamfunction at the same locations. Light (dark) shading indicates clockwise (counterclockwise) flow. Parameters: $\tau=0.5$ and $S=-0.1$.

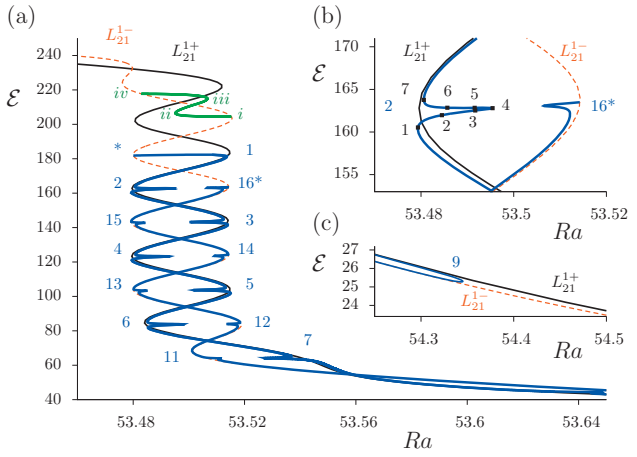

FIG. 13. (Color) (a) Global view of the $L_{21}^{1\pm}$ snaking branches together with two tertiary branches of stationary states (in blue and green) connecting L_{21}^{1-} to itself. The blue tertiary branch extends between the two locations on L_{21}^{1-} denoted by *. The (blue) integers denote the locations of saddle-nodes on L_{21}^{1-} used in Fig. 15 to label the corresponding profiles on the tertiary solution branch. Solutions on the other tertiary branch (green) at locations indicated by green roman numerals are shown in Fig. 16. (b) Detail of the region near saddle-node 2; the (black) integers denote locations corresponding to the solutions shown in Fig. 14. (c) The small amplitude part of the (blue) tertiary branch. Parameters: $\tau=0.5$ and $S=-0.1$.

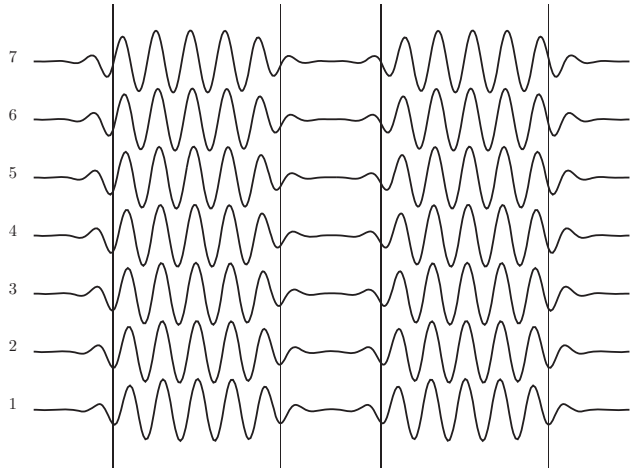

FIG. 14. Line plots showing the midplane vertical velocity $w(x,z=1/2)$ along the tertiary two-pulse (blue) branch in Fig. 13(a) in the cusp region near location 2. Profiles correspond to the numbered locations in Fig. 13(b). The vertical lines indicate alignment of successive profiles. Parameters: $\tau=0.5$ and $S=-0.1$.

In contrast, Fig. 17 shows tertiary branches of steady states connecting the branch L_{21}^{1+} to itself. These branches have a characteristic S shape and consist of solutions along the rungs connecting L_{21}^{1+} to L_{21}^{1-} together with a segment within which the solution resembles an L_{21}^{1-} state very closely. Figure 18 provides an indication of the changes in the solution profile as one traverses the S shape from bottom to top.

V. RESULTS: $\tau=0.05$ AND $S=-0.01$

In this section we present the corresponding results for case (b): $\tau=0.05$ and $S=-0.01$, albeit more briefly. Figure 19 shows the structure of the basic periodic states as a function of the Rayleigh number. For these parameter values P_{20} again bifurcates first, but this time P_{19} is second. Observe that the saddle-node on P_{16} now lies between those on P_{17} and P_{18}, thereby "breaking" the order observed in Fig. 3.

Figure 20 shows some of the secondary branches connecting the periodic states in Fig. 19, with detailed behavior shown in Fig. 21. As in Fig. 4 these take the form of both single and two-pulse states. However, in contrast to Fig. 4 the states L_{20}^{2+} and L_{20}^{2-} terminate on different periodic branches, a possibility studied in detail[10,13] using both SH23 and SH35. Moreover, the snaking region of $L_{20}^{2\pm}$ [Figs. 21(b) and 21(c)] has a much different shape from the classical snaking region exhibited by the single pulse states $L_{20}^{1\pm}$ [Fig. 21(a)]. As in Fig. 5 the width of the snaking executed by odd parity states is slightly narrower than that executed by even parity states [Fig. 21(a)]. In contrast, the snaking structure associated with the $L_{20}^{2\pm}$ states is incomplete [Figs. 21(b) and 21(c)], and its upper tip extends far toward larger values of Ra. This type of behavior, while uncommon, has also been observed in other systems. For example, in natural doubly diffusive convection,[10] the wavenumber change across the pinning region is sufficiently large that it is energetically favorable for the system to incorporate a defect in the structure instead of terminating on a periodic state with the incorrect wavelength. In such circumstances, the snaking branch may turn continuously into a mixed mode state that bifurcates from one of the periodic states and may fail to terminate on a periodic state altogether. In the present example, the snaking branches follow such a mixed mode branch to larger amplitude before turning around and connecting to P_{16} (L_{20}^{2+}) or P_{18} (L_{20}^{2-}). The mechanism whereby two snaking branches originating in the same bifurcation terminate on distinct periodic states was also first identified in the context of natural doubly diffusive convection.[10]

In Fig. 22 we show the details of an additional pair of snaking branches labeled $L_{19}^{1\pm}$ (Fig. 20). These branches correspond to different two-pulse states, each consisting of two midplane reflection-related states of identical parity, either even (L_{19}^{1+}) or odd (L_{19}^{1-}). The resulting snaking structure is

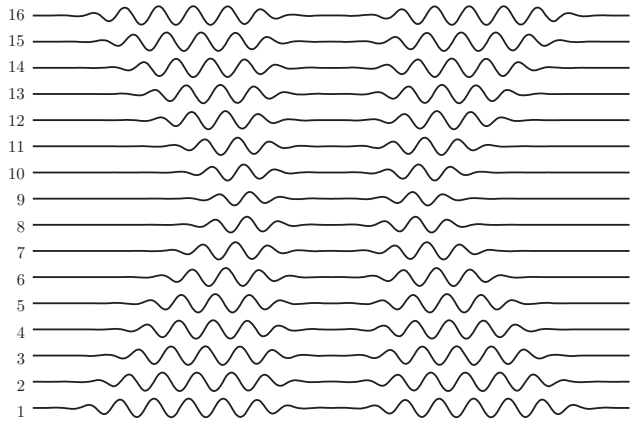

FIG. 15. Tertiary two-pulse states: line plots showing the midplane vertical velocity $w(x,z=1/2)$ at locations nearest to the saddle-nodes on $L_{21}^{1\pm}$, labeled by integers as in Fig. 13. Parameters: $\tau=0.5$ and $S=-0.1$.

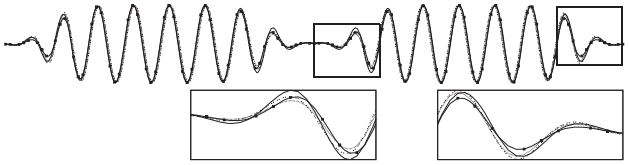

FIG. 16. Line plots showing the midplane vertical velocity $w(x,z=1/2)$ along the tertiary two-pulse (green) branch in Fig. 13(a) at locations (i)–(iv). Label (i): solid line with points; label (ii): dotted line; label (iii): broken line; and label (iv): solid line. Lower panels show enlargements of the boxed regions in the upper panel. Parameters: $\tau=0.5$ and $S=-0.1$.

inclined and does not follow either $L_{20}^{1\pm}$ or $L_{20}^{2\pm}$. Figure 23 superposes the results for $L_{19}^{1\pm}$ and $L_{20}^{2\pm}$ and includes several tertiary branches as well. The top panel shows a pair of S-shaped branches connecting L_{19}^{1+} to itself and a similar S-shaped structure connecting L_{19}^{1-} to itself, together with appropriate enlargements. The lower panel shows a pair of similar S-shaped tertiary branches connecting L_{20}^{2+} to L_{19}^{1-} (green and red tertiary branches). These interconnections also exhibit cusplike structures arising from the breakup of the rung states, much as in Fig. 13, although here the cusps are difficult to discern. The breakup of the rung states also creates the isolalike blue tertiary branch; this branch also connects L_{20}^{2+} to L_{19}^{1-}.

VI. THEORETICAL INTERPRETATION

Two-pulse states in model equations such as SH23 in one spatial dimension have been studied before.[17–20] In a periodic domain of period Γ, the following solutions are found:

- solutions consisting of identical equidistant structures,
- solutions consisting of "identical" but nonequidistant structures, and
- solutions consisting of nonidentical structures.

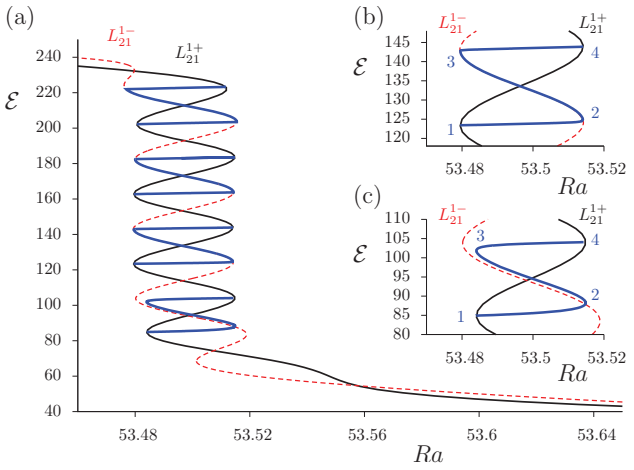

FIG. 17. (Color online) (a) Global view of the $L_{21}^{1\pm}$ snaking branches together with S-shaped tertiary branches of stationary states (light solid lines) connecting L_{21}^{1+} to itself. The (light solid) integers in the details (b) and (c) denote the location of the solutions shown in Fig. 18. Parameters: $\tau=0.5$ and $S=-0.1$.

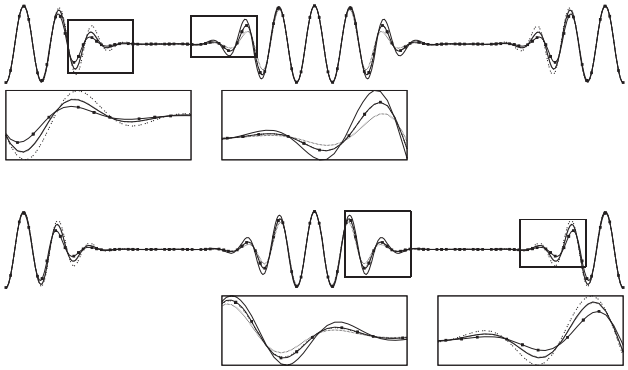

FIG. 18. Line plots showing the midplane vertical velocity $w(x,z=1/2)$ at the locations indicated in Fig. 17. Top (bottom) panels correspond to Fig. 17(b) [Fig. 17(c)]. Label 1: solid line with points; label 2: dotted line; label 3: broken line; and label 4: solid line. Lower panels show enlargements of the boxed regions in the upper panels. Parameters: $\tau=0.5$ and $S=-0.1$.

The former bifurcate from the first branch of periodic states with an even number of wavelengths in the imposed period Γ and snake much as a single pulse state on a periodic domain with period $\Gamma/2$. Thus the branch of identical equidistant structures also terminates near the saddle-node on a branch of periodic states with an even number of wavelengths, but does so after undergoing only approximately half the number of back and forth oscillations executed by the single pulse branch. This is the case in Fig. 5(b). In contrast, nonequidistant pulses do not bifurcate from branches of periodic states and instead form stacks of nested isolas filling the snaking region (Fig. 24). Each isola represents a closed branch of two identical pulses with a given separation different from $\Gamma/2$. Since Γ is finite and the pulses lock to the oscillations in the tails of their profiles, only a finite number of nested isolas is present, and this is so for isolas involving pulses with n oscillations, $n=1,2,\ldots$, with n increasing by one as one proceeds up the stack of isolas from bottom to top (Figs. 24 and 25). Once the width of each

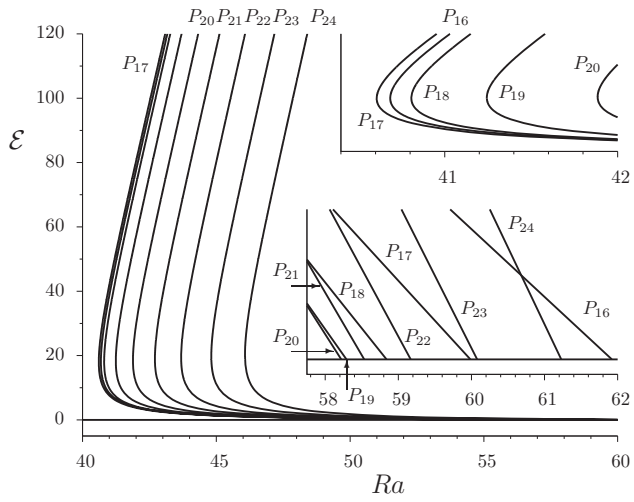

FIG. 19. Bifurcation diagram showing the branches $P_n(n\in[16,24])$ of periodic states as a function of the Rayleigh number Ra. Parameters: $\tau=0.05$ and $S=-0.01$.

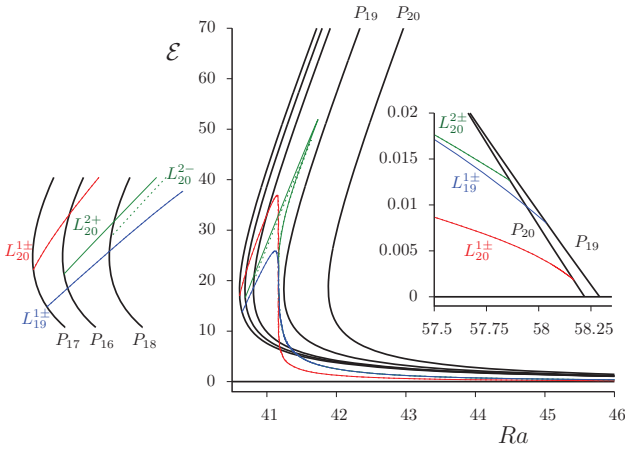

FIG. 20. (Color online) Bifurcation diagram showing some of the secondary branches of localized states connecting the various periodic states. The insets show enlargements of the small amplitude behavior near onset and the termination of the secondary branches near the saddle-nodes on P_{16}, P_{17}, and P_{18}. The classical snaking region near Ra=41.17 is not resolved on the scale of this plot. Parameters: τ=0.05 and S=−0.01.

pulse becomes comparable to $\Gamma/2$, the stack of isolas terminates. Exactly how this happens is not known. We have not computed here such unequally spaced two-pulse states; since these states lie on isolas, numerical continuation is difficult to initialize unless one finds a stable state of this type using time-stepping from a suitably selected initial condition. Other numerical issues in following these isola states are discussed in Ref. 20.

We emphasize that each pulse within the equidistant states in Fig. 5(b) is itself symmetric with respect to either R_1 (about a suitable origin) or $R_2\circ R_1$ (about a suitable origin). These symmetry properties imply that on its own, neither pulse drifts. When combined into equidistant two-pulse states such as $L_{20}^{2\pm}$, the distortion of a pulse due to pulses on either side preserves these symmetries, and the resulting two-pulse states are therefore also stationary. Moreover,

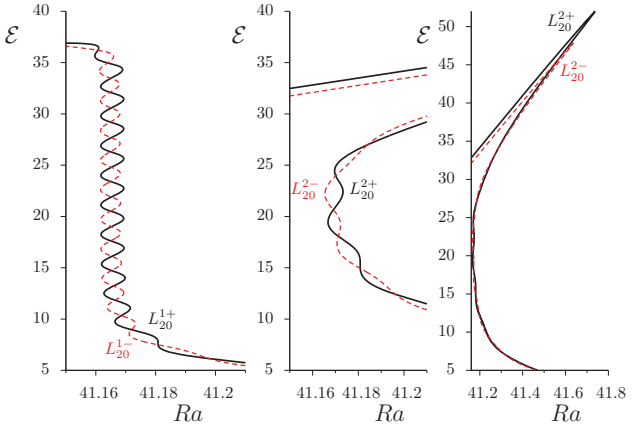

FIG. 21. (Color online) Detail of the snaking region in Fig. 20. Left: snaking of the single pulse states $L_{20}^{1\pm}$; solid (dashed) line represents even (odd) parity states L_{20}^{1+} (L_{20}^{1-}). The L_{20}^{1-} snaking region is narrower than the L_{20}^{1+} snaking region. Center and right: snaking of two-pulse states with phases ϕ=(0,0) (L_{20}^{2+}, solid line) and ϕ=($\pi/2,\pi/2$) (L_{20}^{2-}, dashed line). Parameters: τ=0.05 and S=−0.01.

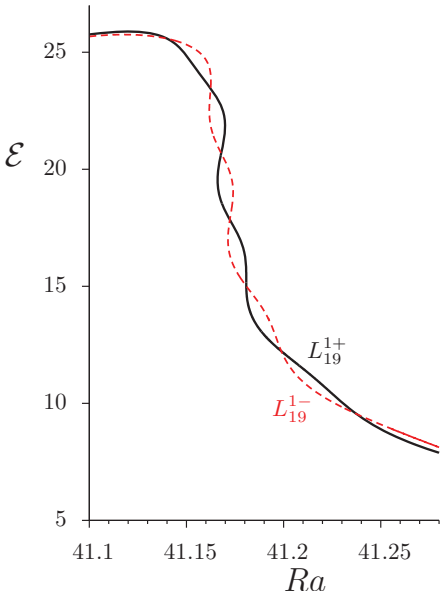

FIG. 22. (Color online) Further detail of the snaking region in Fig. 20. Snaking of two-pulse states with phases ϕ=(0,π) (L_{19}^{1+}, solid line) and ϕ=($\pi/2,3\pi/2$) (L_{19}^{1-}, dashed line). Parameters: τ=0.05 and S=−0.01.

bound states of types (0,0) and (0,π) consisting of identical states with unequal separations are R_1-symmetric and $R_2\circ R_1$-symmetric, respectively, in both cases with respect to the midpoint of each bound pair. Thus we expect isolas of unequally spaced steady states of either type, in addition to the snaking branches L_{20}^{2+} [Fig. 5(b)] and L_{21}^{1+} (Fig. 10) of equidistant steady states of either type. Equidistant ($\pi/2,\pi/2$) and ($\pi/2,3\pi/2$) states are likewise $R_2\circ R_1$- and

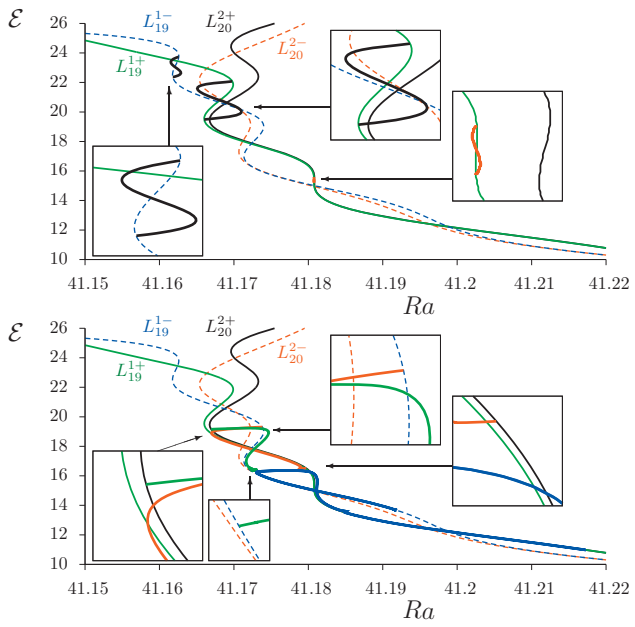

FIG. 23. (Color) Global view of the $L_{19}^{1\pm}$ and $L_{20}^{2\pm}$ snaking branches with solid (broken) lines indicating +(−) states. Upper panel shows S-shaped tertiary branches connecting L_{19}^{1+} to itself and L_{19}^{1-} to itself. Lower panel shows tertiary branches connecting L_{19}^{1-} to L_{20}^{2+}. Parameters: τ=0.05 and S=−0.01.

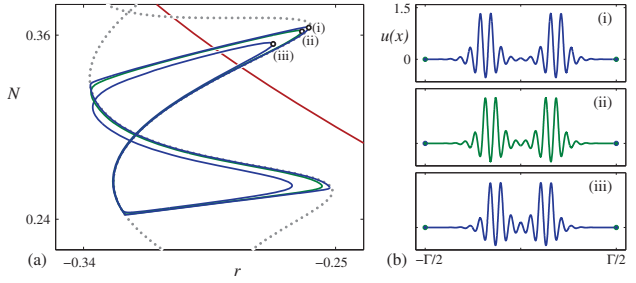

FIG. 24. (Color online) (a) Bifurcation diagram showing isolas of symmetric two-pulse states in SH23. The nested isolas correspond to fixed pulse width as the pulse separation varies. For reference, the snaking branches of equidistant two-pulse states are plotted as dotted lines. The light solid line is a branch of unstable periodic states. (b) Profiles at the points labeled in the bifurcation diagram. Parameters: $b_2=1.8$ and $\Gamma=118$. Reprinted with permission from J. Burke and E. Knobloch, Discrete Contin. Dyn. Syst. Supplement **2009**, 109. Copyright © 2009, American Institute of Mathematical Sciences.

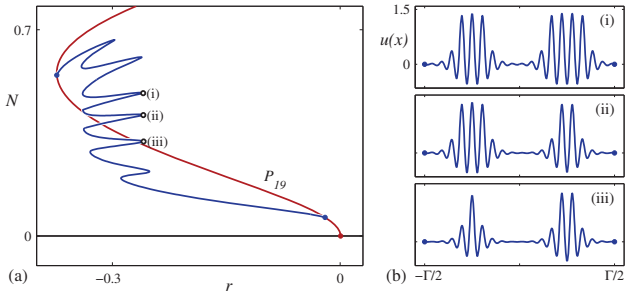

FIG. 26. (Color online) (a) Bifurcation diagram showing a branch of nonsymmetric two-pulse localized states in SH23, which emerges from and terminates on the spatially periodic branch P_{19}. (b) Profiles at the points labeled in the bifurcation diagram. Parameters: $b_2=1.8$ and $\Gamma=118$. Reprinted with permission from J. Burke and E. Knobloch, Discrete Contin. Dyn. Syst. Supplement **2009**, 109. Copyright © 2009, American Institute of Mathematical Sciences.

R_1-symmetric, and these symmetries persist for unequal separations of identical pulses as well. Thus we expect nonequidistant steady states of either type to also lie on isolas, in addition to the snaking branches L_{20}^{2-} [Fig. 5(b)] and L_{21}^{1-} (Fig. 10) of equidistant steady states of either type.

We remark that, within SH23, one also finds snaking branches of *unequal* pulses that bifurcate from the first branch of periodic states with an odd number of wavelengths in the period Γ (Fig. 26). In nonvariational systems, states of this type necessarily drift. We have not computed similar states in the present problem, although there is every indication that such states are in fact present. Instead we have focused on the *steady* states that bifurcate from such branches, here P_{21} or P_{19}, instead of the primary branch, here P_{20} (Figs. 4 and 20). These states necessarily consist of identical equidistant states with either R_1 or $R_2\circ R_1$ symmetry and hence do not drift.

The states $L_{21}^{1\pm}$ consist of two equidistant pulses of the same parity but opposite signs (Figs. 11 and 12). Tertiary bifurcations from these states create new steady states provided the resulting state remains reflection-symmetric. To understand the nature of these states, we examine the solutions on the half-domain $0\le x\le\Gamma/2$, identify possible bifurcations, and then construct a reflection-symmetric state on the full domain $-\Gamma/2\le x\le\Gamma/2$ by putting the bifurcated state back-to-back with its mirror image in $x=0$. The state L_{21}^{1+} in Fig. 11, restricted to $0\le x\le\Gamma/2$, satisfies NBCs at $x=0$, $\Gamma/2$. On this domain the state has the reflection symmetry $R_2\circ R_{\Gamma/4}$, where $R_{\Gamma/4}$ represents a reflection in $x=\Gamma/4$. It follows that aside from saddle-node bifurcations (Fig. 10), the L_{21}^{1+} state can also undergo symmetry-breaking pitchfork bifurcations. These bifurcations do take place (Fig. 17) and lead to the solutions shown in Fig. 18. Because of the broken reflection symmetry, these solutions, if posed on a periodic domain of length $\Gamma/2$, would drift; however when put back-to-back with the mirror image obtained by reflection in $x=0$, the reconstructed state becomes reflection-symmetric and so is stationary with PBC on the domain Γ. The resulting tertiary branches form S-shaped curves [Figs. 17(b) and 17(c)] parts of which hug the rung states, while the middle part hugs the L_{21}^{1-} branch.

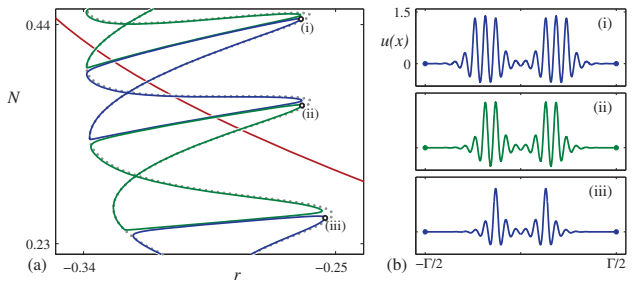

FIG. 25. (Color online) (a) Bifurcation diagram showing isolas of symmetric two-pulse states in SH23. The stack of isolas corresponds to fixed pulse separation as the individual pulse width grows. (b) Profiles at the points labeled in the bifurcation diagram. Parameters: $b_2=1.8$ and $\Gamma=118$. Reprinted with permission from J. Burke and E. Knobloch, Discrete Contin. Dyn. Syst. Supplement **2009**, 109. Copyright © 2009, American Institute of Mathematical Sciences.

The L_{21}^{1-} state restricted to $0\le x\le\Gamma/2$ also satisfies NBC and is likewise invariant under $R_2\circ R_{\Gamma/4}$. Once again, aside from saddle-node bifurcations, symmetry-breaking bifurcations generate states of the type observed in Fig. 15. With PBC on a domain $\Gamma/2$, these states would drift, but the reconstructed solution on the original domain seen in Fig. 15 is reflection-symmetric and so corresponds to steady states. This time the tertiary branches have a very spiky form, where adjacent parts of the branch hug rung states. There are two types of these cusps, longer ones that form when the tertiary branch hugs the L_{21}^{1+} branch and shorter ones when it hugs the L_{21}^{1-} branch. These structures resemble similar behavior identified in SH35 when the boundary conditions on the domain Γ are changed[13] from PBC to NBC; the S-shaped branches resembling those bifurcating from L_{21}^{1+} arise when the boundary conditions are changed to Dirichlet boundary conditions (DBCs) instead (Fig. 27). These results are evidently related to the behavior reported in Figs. 13 and 17. This is because the centered L_{21}^{1+} states in Fig. 11 do in fact satisfy DBC on $-\Gamma/4\le x\le\Gamma/4$, while the L_{21}^{1-} states in Fig. 12 satisfy NBC on $0\le x\le\Gamma/2$. Thus in both SH35 and the present system, the observed structure of the tertiary

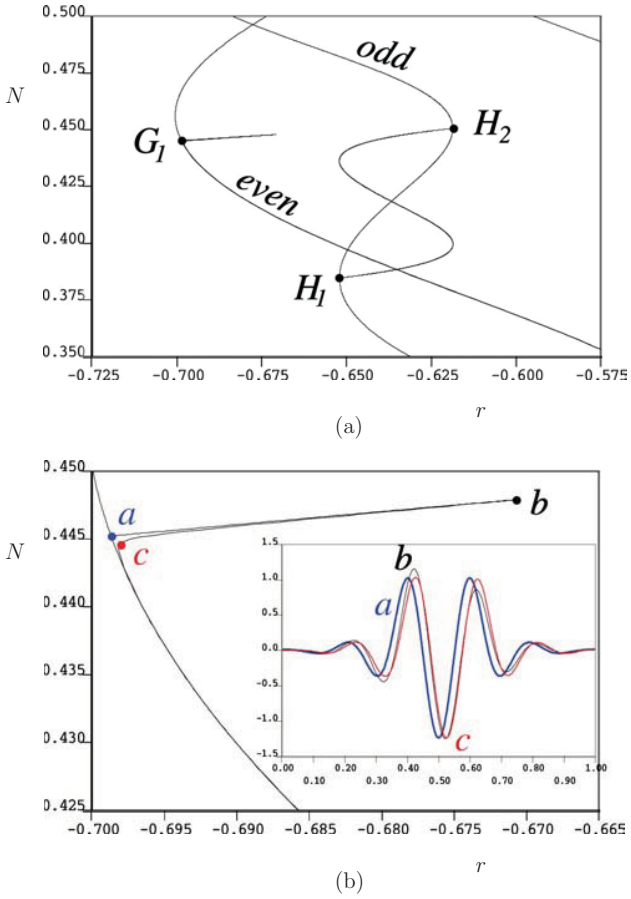

FIG. 27. (Color online) Superposition of the DBC and NBC bifurcation diagrams for SH35. (a) The even parity branch undergoes a pitchfork bifurcation at G_1 producing a narrow bubble of asymmetric states; this bubble closes at larger r. The odd parity branch also produces a bubble of asymmetric states between pitchfork bifurcations at H_1 and H_2. (b) Enlargement of (a) with an inset plot of the localized states at points a, b, and c. Point a in (b) is the same as point G_1 in (a). Parameters: $b_3=2$ and $\Gamma=10\pi$. From J. H. P. Dawes, SIAM J. Appl. Dyn. Syst. **8**, 909 (2009). Copyright © 2009 Society for Industrial and Applied Mathematics. Reprinted with permission. All rights reserved.

branches follows the geometrical mechanism described in Ref. 24.

The above arguments apply to case (b) as well (Fig. 23): one finds S-shaped tertiary branches connecting L_{19}^{1+} to itself as well as S-shaped tertiary branches connecting L_{19}^{1-} to itself. In addition, one now finds tertiary branches that connect L_{19}^{1-} to L_{20}^{2+}. Whether similar connections are present in SH35 is unknown.

It will have been noticed that while the single pulse even and odd parity convectons snake in more or less the same interval in Ra, the widths of the snaking intervals are not the same: the snaking interval for the odd parity states is narrower than that of the even parity states, an observation that also applies to standard binary fluid convection.[2] This is a consequence of the fact that the odd parity states *pump* concentration from one side of the convecton to the other. In fact, the corresponding saddle-nodes align very well along the *left* boundary of the snaking region corresponding to a tangency between the unstable manifold of the conduction state and the center-stable manifold of the periodic state with wavelength λ_c. This alignment occurs because at this value of the Rayleigh number, new cells are being nucleated and are still too weak to entrain concentration into the convecton. Thus at this Ra, the mean concentration inside and outside the odd convectons is the same, and this is so for the even convectons as well. However, as one follows the snaking branch upward to the next saddle-node at the *right* boundary of the snaking region, the new cells on either side strengthen in amplitude to the characteristic amplitude of the existing convection cells. For even parity convectons, this implies that the cells at either end of the convecton either both entrain high concentration fluid into the convecton or that both entrain low concentration fluid. Thus the concentration inside is either larger or smaller than average, depending on the direction of the flow in the outermost cells.[2] In an odd convecton, however, the cells at both ends rotate in the same direction. As a result concentration is entrained at one end and rejected at the other, i.e., there is net pumping of concentration across the structure, and this pumping sets up a concentration gradient between adjacent odd convectons. This is the case for single pulse states on a periodic domain and also for two-pulse states of $(\pi/2,\pi/2)$ type such as L_{20}^{2-}. This is the reason behind the different widths of the snaking region of $L_{20}^{2\pm}$. In contrast, if one places odd parity convectons back-to-back as in the $(\pi/2,3\pi/2)$ state L_{21}^{1-} (Fig. 12), both structures pump toward one another, thereby raising the concentration between them to an above average value while depleting it outside, i.e., between $(3\pi/2,\pi/2)$ (or vice versa). In such a situation, each convecton finds itself embedded in an inhomogeneous background, and no net concentration flux is present. The effect of the resulting bound pair of convectons is thus identical to that of a single even parity state. It is for this reason that the snaking regions of $L_{21}^{1\pm}$ are identical (Fig. 10), while those of $L_{20}^{1\pm}$ or $L_{20}^{2\pm}$ are not. In the presence of impermeable walls, the same argument applies (despite the different velocity boundary conditions), and the width of the snaking region for odd and even convectons in closed containers is therefore the same, in contrast to the case with PBC.[27,35] This all-important pumping effect is not captured by Swift–Hohenberg type models.

VII. CONCLUSIONS

In this paper we have explored the bifurcation behavior of a relatively simple convection problem—binary convection in a porous medium. Like other problems of this type, this problem exhibits a subcritical primary instability to a spatially periodic state. However, because of the simpler boundary conditions on the velocity field, the problem is amenable to more detailed numerical continuation, particularly if the (inverse) Lewis number τ is not too small. As a result we have been able to identify much new behavior associated with the presence of bistability in this system. In particular we have verified that the behavior of single pulse states follows the snaking behavior observed in other fluid systems[2,9] and familiar from studies of variational systems such as the SHE.[14] In addition, we have been able to study two-pulse states, i.e., bound states of two convectons. We

have identified a variety of different bound states depending on the spatial phase ϕ of the constituent convectons and showed that these also fall on snaking branches. Although we have focused on the properties of equidistant two-pulse states, we have argued for the presence of a multiplicity of other states of this type that lie on isolas, i.e., disconnected solution branches. Finally, we have identified a variety of tertiary branches consisting of bound states of asymmetric pulses and showed that these also snake. These states connect the equidistant two-pulse branches either to themselves or to one another in a manner reminiscent of the single pulse rung states in the snake-and-ladders structure of the single pulse snaking region.[12,24] The details of this structure remain to be elucidated, however, since our techniques only allow us to compute steady states, and as we have argued, many of these states will in fact drift.

We believe that the states we have computed here are more than a curiosity. Indeed our calculations demonstrate vividly the richness of even very simple partial differential equations and in particular of the region in parameter space called the snaking or pinning region. This region not only consists of the snake-and-ladders structure of single pulse states but, as we have shown here, also includes the corresponding structure associated with two-pulse states and presumably higher order bound structures as well. This immensely complex region appears to be a general property of reversible bistable systems in which a stable homogeneous state coexists with a structured or heterogeneous state and is associated with transverse intersections of their stable and unstable manifolds when viewed as a dynamical system evolving in space from $x=-\infty$ to $x=\infty$. Thus it is no surprise that related two-pulse states are present in binary fluid convection as well.[36]

ACKNOWLEDGMENTS

This work was supported by the National Science Foundation under Grant No. DMS-0908102 and the Berkeley-France Fund.

[1] O. Batiste and E. Knobloch, "Simulations of localized states of stationary convection in ^{3}He–^{4}He mixtures," Phys. Rev. Lett. **95**, 244501 (2005).
[2] O. Batiste, E. Knobloch, A. Alonso, and I. Mercader, "Spatially localized binary fluid convection," J. Fluid Mech. **560**, 149 (2006).
[3] S. Blanchflower, "Magnetohydrodynamic convectons," Phys. Lett. A **261**, 74 (1999).
[4] S. Blanchflower and N. Weiss, "Three-dimensional magnetohydrodynamic convectons," Phys. Lett. A **294**, 297 (2002).
[5] J. H. P. Dawes, "Localized convection cells in the presence of a vertical magnetic field," J. Fluid Mech. **570**, 385 (2007).
[6] K. Ghorayeb, "Etude des écoulements de convection thermosolutale en cavité rectangulaire," Ph.D. thesis, Université Paul Sabatier, Toulouse 3, France, 1997.
[7] K. Ghorayeb and A. Mojtabi, "Double diffusive convection in a vertical rectangular cavity," Phys. Fluids **9**, 2339 (1997).
[8] A. Bergeon and E. Knobloch, "Periodic and localized states in natural doubly diffusive convection," Physica D **237**, 1139 (2008).
[9] A. Bergeon and E. Knobloch, "Spatially localized states in natural doubly diffusive convection," Phys. Fluids **20**, 034102 (2008).
[10] A. Bergeon, J. Burke, E. Knobloch, and I. Mercader, "Eckhaus instability and homoclinic snaking," Phys. Rev. E **78**, 046201 (2008).
[11] T. M. Schneider, J. F. Gibson, and J. Burke, "Snakes and ladders: Localized solutions of plane Couette flow," Phys. Rev. Lett. **104**, 104501 (2010).
[12] J. Burke and E. Knobloch, "Snakes and ladders: Localized states in the Swift–Hohenberg equation," Phys. Lett. A **360**, 681 (2007).
[13] J. H. P. Dawes, "Modulated and localized states in a finite domain," SIAM J. Appl. Dyn. Syst. **8**, 909 (2009).
[14] J. Burke and E. Knobloch, "Homoclinic snaking: Structure and stability," Chaos **17**, 037102 (2007).
[15] P. Coullet, C. Riera, and C. Tresser, "A new approach to data storage using localized structures," Chaos **14**, 193 (2004).
[16] J. Burke and E. Knobloch, "Localized states in the generalized Swift–Hohenberg equation," Phys. Rev. E **73**, 056211 (2006).
[17] G. H. M. van der Heijden, A. R. Champneys, and J. M. T. Thompson, "Spatially complex localisation in twisted elastic rods constrained to a cylinder," Int. J. Solids Struct. **39**, 1863 (2002).
[18] M. K. Wadee, C. D. Coman, and A. P. Bassom, "Solitary wave interaction phenomena in a strut-buckling model incorporating restabilisation," Physica D **163**, 26 (2002).
[19] J. Knobloch and T. Wagenknecht, "Snaking of multiple homoclinic orbits in reversible systems," SIAM J. Appl. Dyn. Syst. **7**, 1397 (2008).
[20] J. Burke and E. Knobloch, "Multipulse states in the Swift–Hohenberg equation," Discrete Contin. Dyn. Syst. Supplement **2009**, 109.
[21] G. W. Hunt, M. A. Peletier, A. R. Champneys, P. D. Woods, M. Ahmer Wadee, C. J. Budd, and G. J. Lord, "Cellular buckling of long structures," Nonlinear Dyn. **21**, 3 (2000).
[22] G. Kozyreff and S. J. Chapman, "Asymptotics of large bound states of localized structures," Phys. Rev. Lett. **97**, 044502 (2006).
[23] S. J. Chapman and G. Kozyreff, "Exponential asymptotics of localized patterns and snaking bifurcation diagrams," Physica D **238**, 319 (2009).
[24] M. Beck, J. Knobloch, D. J. B. Lloyd, B. Sandstede, and T. Wagenknecht, "Snakes, ladders and isolas of localized patterns," SIAM J. Math. Anal. **41**, 936 (2009).
[25] P. D. Woods and A. R. Champneys, "Heteroclinic tangles and homoclinic snaking in the unfolding of a degenerate Hamiltonian–Hopf bifurcation," Physica D **129**, 147 (1999).
[26] P. Coullet, C. Riera, and C. Tresser, "Stable static localized structures in one dimension," Phys. Rev. Lett. **84**, 3069 (2000).
[27] I. Mercader, O. Batiste, A. Alonso, and E. Knobloch, "Convectons in periodic and bounded domains," Fluid Dyn. Res. **42**, 025505 (2010).
[28] D. A. Nield and A. Bejan, *Convection in Porous Media* (Springer, New York, 1992).
[29] A. Mojtabi and M.-C. Charrier–Mojtabi, "Double-diffusive convection in porous media," in *Handbook of Porous Media*, 2nd ed., edited by K. Vafai (Taylor & Francis, London, 2005), Chap. 7, p. 269.
[30] D. A. Bratsun, D. V. Lyubimov, and B. Roux, "Co-symmetry breakdown in problems of thermal convection in porous medium," Physica D **82**, 398 (1995).
[31] L. S. Tuckerman, "Steady-state solving via Stokes preconditioning: Recursion relations for elliptic operators," in *Proceedings of the 11th International Conference on Numerical Methods in Fluid Dynamics*, edited by D. L. Dwoyer, M. Y. Hussaini, and R. G. Voigt (Springer, New York, 1989), p. 573.
[32] C. K. Mamun and L. S. Tuckerman, "Asymmetry and Hopf bifurcation in spherical Couette flow," Phys. Fluids **7**, 80 (1995).
[33] M. Deville, P. F. Fischer, and E. H. Mund, *High-Order Methods for Incompressible Fluid Flow* (Cambridge University Press, Cambridge, 2002).
[34] M. C. Charrier-Mojtabi, B. Elhajjar, and A. Mojtabi, "Analytical and numerical stability analysis of Soret-driven convection in a horizontal porous layer," Phys. Fluids **19**, 124104 (2007).
[35] I. Mercader, O. Batiste, A. Alonso, and E. Knobloch, "Localized pinning states in closed containers: Homoclinic snaking without bistability," Phys. Rev. E **80**, 025201(R) (2009).
[36] A. Alonso, O. Batiste, E. Knobloch, and I. Mercader, "Convectons," in *Localized States in Physics: Solitons and Patterns*, edited by O. Descalzi (Springer, New York, 2010).